Rheo-optics of Equilibrium Polymer Solutions: Wormlike Micelles in Elongational Flow in a Microfluidic Cross-Slot

Jai A. Pathak*,† and Steven D. Hudson*

National Institute of Standards and Technology, Polymers Division, Gaithersburg, Maryland 20899-8542

Received June 18, 2006; Revised Manuscript Received September 19, 2006

ABSTRACT: The rheo-optical analysis of polymer solutions and melts is a critical tool in elucidating their molecular response to flow fields. We therefore evaluate the measurement of flow-induced birefringence (orientation) under extension in microfluidic cross-slots, whose flow kinematics was examined by microparticle image velocimetry. The effects of planar extension on the (non)linear viscoelasticity of wormlike micellar surfactant solutions (comprising either cetyltrimethylammonium bromide or cetylpyridinium chloride in aqueous sodium salicylate) were measured. The effect of wall shear was found to be negligible compared to extension. The birefringence is linear (indicating the validity of the stress−optical rule) for very small extensional Weissenberg numbers, as expected. This rule fails, however, when a sharp birefringence band appears at modest Weissenberg number (indicating the alignment of wormlike micelles along the outflow direction). Experiments that measure average birefringence may misidentify the point of failure of the stress−optical rule. These bands also scatter light and appear in transmittance images, yet with distinctive features. At higher flow rates, the birefringent band broadens after the peak retardation saturates, but the transmittance band remains narrow and eventually the flow becomes asymmetric. This asymmetric transition is elasticity-induced, and no shear banding is observed by particle velocimetry: the velocity profiles remain linear, while the flow becomes asymmetric. These phenomena are common to both fluids studied, but the stress−optical coefficient and the Weissenberg numbers at saturated birefringence differ quantitatively, possibly due to differences in micellar length and scission kinetics, as determined from linear viscoelastic measurements.

I. Introduction

Sir Geoffrey Taylor's pioneering invention of the four-roll mill (FRM)[1,2] has afforded generations of rheologists an elegant means of creating extensional and other mixed flows. FRM's have been applied to studies on emulsion droplet deformation,[3,4] and Keller et al.[5] applied it in their seminal studies of flow-induced birefringence (FIB) in polymer solutions undergoing elongational flows. While the FRM is a good means of creating extensional flows, its analogue, the cross-slot (opposing fluid streams flowing through crossed slots to produce extensional flow with a well-defined stagnation point, SP, at the center), is easier to build and control. Workers have used cross-slots to study polymer chain scission,[6−10] chain deformation/scission in turbulent drag reduction flows,[11−13] and chain conformation hysteresis[14] associated with the coil−stretch transition.[15]

In earlier work, we built a microfluidic cross-slot and demonstrated its unprecedented ability to control the frame-invariant flow type parameter ξ.[16] We used an objective flow classification, based on that of Astarita.[17]

$$\xi = \frac{\underline{\underline{D}}:\underline{\underline{D}} + \underline{\underline{W}}:\underline{\underline{W}}}{\underline{\underline{D}}:\underline{\underline{D}} - \underline{\underline{W}}:\underline{\underline{W}} + 2\sqrt{(\underline{\underline{D}}:\underline{\underline{D}})(\underline{\underline{W}}:\underline{\underline{W}})}} \qquad (1)$$

$\underline{\underline{D}}$ and $\underline{\underline{W}}$ are the tensorial stretching and rotation rates, respectively. $\underline{\underline{W}}$ is specified relative to the material rotation of the principal axes of $\underline{\underline{D}}$. $\xi = 1$ and $\xi = -1$ correspond to pure straining (irrotational or extensional) flow and pure rotational flow, respectively. Simple shear flow comprises equal parts of extension and rotation ($\xi = 0$).[18] Flows corresponding to ξ's other than −1 and 1 are called "mixed". While the FRM cannot produce simple shear, our cross-slot can produce nearly pure rotation to pure extension, *including simple shear*. In our previous report[16] we demonstrated that channel aspect ratio (height/width) has a significant effect on accessible ξ's. Therefore, we use soft lithography microfluidic fabrication techniques here to fabricate channels with aspect ratio of ≈0.5, which can give $\xi = 1$. Extensional flows strongly deform polymer chains,[19] motivating our choice of planar elongational flow (PEF). Birefringence, the anisotropy of the refractive index tensor, gives rise to a phase difference of polarized light passing through optically anisotropic fluids, and it has been widely used to study dynamics[20] of polymers and complex fluids.[21]

An obvious advantage of microfluidic flows is that they need smaller fluid volumes,[22,23] a key concern in experiments on exotic fluids. Microfluidic channels are fabricated using standard soft-lithography methods,[24−26] which enable easy adjustment of channel dimensions, an important capability for analysis of viscoelastic fluid flows. By this means, one controls the relative magnitudes of the Weissenberg number (*Wi*)[27] and Reynolds (*Re*) number in the *Wi*−*Re* parameter space. In this study, only elasticity is at play, but in certain other viscoelastic flows,[28] both elasticity and inertia can contribute significantly.

Wormlike micellar fluids are highly viscoelastic,[29,30] and they are also commercially applied as viscosity modifiers, as drag reducing agents, and in enhanced oil recovery. They are treated as equilibrium polymers due to reversible scission and fusion of micellar chains that are governed by equilibrium between fusion and scission kinetics. Semidilute wormlike micellar solutions display linear viscoelasticity (LVE) that is markedly similar to solutions of monodisperse polymers.[29−32] They also exhibit shear banding in shear flows[33−46] and possess large FIB[46−51] and large normal stresses. The relationship between

* E-mail: Jai.Pathak@nrl.navy.mil, Steven.Hudson@nist.gov.
† Current address: Polymer Physics Section, U.S. Naval Research Laboratory, Washington, DC 20375-5342.

10.1021/ma061355r
Published on Web 11/17/2006

shear banding and birefringence has been investigated.[33,39,42,52] While the linear and nonlinear viscoelasticity of wormlike micelles,[53,54] including FIB,[39,42,46,48−51,55,56] have been studied extensively, the preponderance of these studies has been unsurprisingly limited to simple shear flow, which is easier to create than extensional flows, especially in non-Newtonian fluids. Wormlike micelles have been studied in commercial opposed jets devices[57−60] that create uniaxial extensional flow (UEF), with somewhat different kinematics from PEF. Yesilata et al.[61] have recently published the results of a study of nonlinear shear and extensional flow (in a capillary breakup rheometer[62]).

We seek to answer some well-defined questions here. What is the response of wormlike micelles to PEF? What are the conditions where the stress−optical rule (SOR) is upheld/violated? Is any mechanical instability seen in the response of wormlike micelles to PEF? If so, what can we determine about the mechanism and/or the kinetics of the instability? The fluid experiences shear deformation next to the walls in the inlet channel of the device (Poiseuille flow), and so we perform FIB experiments upstream of the SP to compare the response in extensional and shear flow. We also experimentally investigate the spatiotemporal relaxation of birefringence with increasing distance from the SP along the outflow axis (i.e., downstream of the SP).

To demarcate the emphasis of our work from recently published similar ones, we note that while Kato et al.[63] have created PEF for cetyltrimethylammonium bromide (CTAB)/sodium salicylate (NaSal) solutions in a FRM, their work lacks sufficient detail to address the questions raised here. They also made birefringence measurements on the same system in a 2D converging channel[64] but made an *a priori* assumption about the validity of the stress−optical rule[65] (SOR) in elongation. Since elongational flows are strong flows, the SOR may fail at modest rates,[66,67] and its validity should be established before application. Also, while Penfold et al.[68] have recently built a macrofluidic cross-slot flow cell and used small-angle neutron scattering (SANS) to study the effect of elongational flow on flow-induced ordering in surfactant micelles, their work emphasized spatially resolved SANS to determine the orientational ordering in their flow cell and to compare it with corresponding effects arising from shear flow. Our primary focus, quite distinct from theirs, is the study of FIB of wormlike micelles in PEF to gain an understanding of their viscoelasticity.

II. Experimental Procedure

A. Microfluidic Device Fabrication. Cabral and Hudson[69] have described the channel fabrication and assembly process in detail. SU-8 photoresist (grade 2075; MicroChem Inc.[70]) was also used here to prepare a channel of height $h = 530\ \mu$m and sufficiently "small" aspect ratio $h/w = 0.53$ at which $\xi = 1$ can be attained for 3-D Stokes flow in the cross-slot.[16] Background birefringence from the PDMS network in the glass/PDMS microfluidic channel is subtracted by a procedure discussed in section IIC, and wall shear effects are also quantified.

B. Preparation and Rheology of Wormlike Micellar Fluids. Two surfactant solutions were prepared. One was a solution of 30 mmol L^{-1} CTAB/240 mmol L^{-1} NaSal fluid (same concentration and components used by Kadoma and van Egmond[71]). Both components (procured from Sigma-Aldrich) were weighed out directly into a volumetric flask. Deionized water (resistivity = 18.0 $\times 10^6\ \Omega$·cm) was added, and the mixture was dissolved using gentle convection in a 3-D rotator (Labline) over 2−3 days to homogeneity until a uniform appearance free of refractive index gradients was seen throughout the flask. Another solution, 100 mmol L^{-1} cetylpyridinium chloride (CPyCl)/60 mmol L^{-1} NaSal, was also similarly prepared (CPyCl procured from Sigma-Aldrich). The solutions were allowed to then stand for at least 10 days before use.

The angular frequency (ω)-dependent complex modulus $G^*(\omega) = G'(\omega) + iG''(\omega)$ of the CTAB/NaSal solution was reproducibly measured by oscillatory shear (OS) experiments in a strain-controlled ARES low-shear rheometer (Rheometric Scientific) using 25 mm diameter parallel platens; $G'(\omega)$ and $G''(\omega)$ denote the storage and loss moduli, respectively. The applied strain amplitude, determined from strain sweep experiments, produced linear viscoelastic response in the fluid. To prevent sample evaporation, ARES' convection oven was turned off, and the experiment was performed at ambient temperature (22 °C) over only three decades of ω. The sample was visually inspected post-experiment to confirm negligible evaporation.

C. Birefringence Microscope Setup, Procedure, and Data Analysis/Corrections. We performed birefringence measurements on a Metripol birefringence microscope (Oxford Cryosystems), which is based on the Wood and Glazer method.[72] Monochromatic light ($\lambda = 550$ nm) is sent through a rotating polarizer into the sample, then through a quarter wave plate and an analyzer into a CCD camera (10 bit Firewire; Scion CFW-1310M high-resolution; 1360 × 1024 pixels), which measures the light intensity I. Other measured quantities are the phase difference θ between two orthogonally polarized components and the orientation angle ϕ of the sample's principal axis. I, θ, and ϕ are interrelated:[72]

$$I = \frac{1}{2} I_0 [1 + \sin\{2(\omega_{pol}\tau_m - \phi)\}\sin\theta] \qquad (2)$$

I_0 is the transmittance, while ω_{pol} and τ_m denote the polarizer's rotational frequency and the measurement time, respectively. Checks and calibrations performed on the system included alignment and light intensity uniformity check, assessment of optical path polarization state without the sample, and assessment of the camera's dark noise and linear response from 0% to 80% of its dynamic range. A 10× objective lens (NA = 0.25; magnification = 0.47 μm/pixel) was used. The condenser was adjusted so that the effective NA was ∼0.09.

Two 10 mL syringes, filled with the wormlike micellar fluid, were loaded on a syringe pump (Harvard apparatus PHD2000) and connected to the cross-slot device by rigid polyethylene (Intramedic PE-100; Becton Dickinson; i.d. = 0.86 mm; o.d. = 1.52 mm) tubing of minimal length to mitigate compliance effects. The syringe pump response was verifiably free of undesirable pulsation effects that can render a flow unsteady. FIB measurements were checked for reproducibility on two different stock solutions of each wormlike micellar fluid and in two different microfluidic devices. Excellent agreement was seen across respective data sets. Before each measurement the flow was given time to stabilize, and steady birefringence values (ensured by repeating measurements and checking for time invariance) are reported here.

The background sin θ contribution of the PDMS network in the cross-slot device was subtracted from the measured sin θ in the FIB experiments. The magnitude of this contribution varied from one device to another and also with the location on each device. Birefringence measurements were thus made with the *quiescent* wormlike micellar surfactant solution filling the microfluidic device for each region of interest.

All FIB measurements were made at room temperature (22−23 °C) in the channel's midplane, whose location was determined by focusing the microscope on the channel's top and bottom and setting the focus to the dividing plane, where the 3-D flow was quantified to be PEF (see next section). Since the kinematics experienced by the fluid immediately adjacent to the PDMS and glass walls was primarily shear, it is imperative to estimate the contribution to the birefringence arising from wall shear and compare it with the birefringence arising from PEF at the midplane. We accomplished this by using FIB data of Poiseuille flow in the inlet channel upstream of the SP. For FIB measurements downstream of the SP, this weak contribution from wall shear was subtracted.

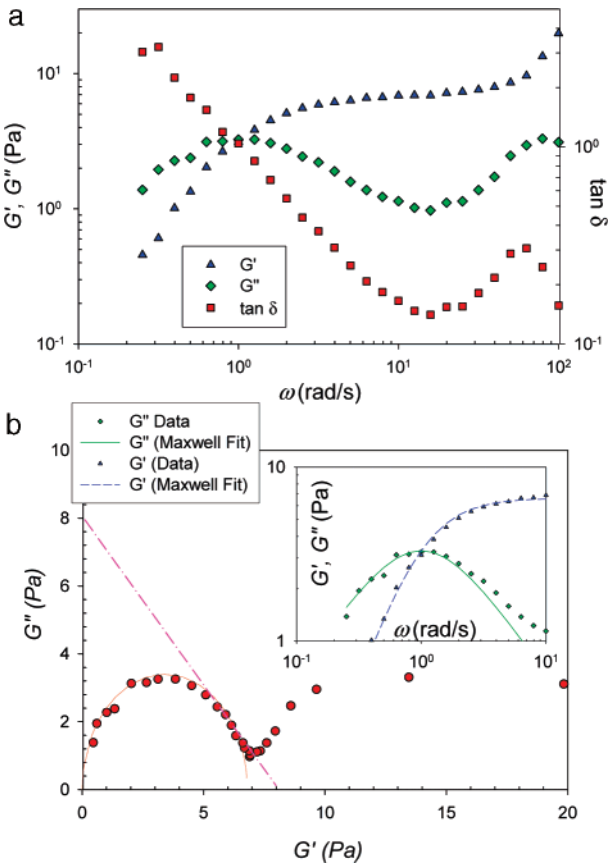

Figure 1. Linear viscoelasticity of the 30 mmol L^{-1} CTAB/240 mmol L^{-1} NaSal solution. (a) $G'(\omega)$, $G''(\omega)$, and tan δ. (b) Cole−Cole−Han plot, where the discrete points are the LVE data, while the smooth curve is a fitted semicircle. The dashed straight line denotes an asymptote with slope = −1. Inset: Maxwell fit (smooth curves) to G' and G'' data signifying the terminal relaxation (discrete points). Standard uncertainties associated with G' and G'' are O(0.1 Pa).

D. μ-PIV. Microparticle image velocimetry (μ-PIV)[73,74] was performed to verify the flow kinematics for the wormlike micellar fluids flowing through the cross-slot devices. 40 μL of a suspension of PS microspheres (Polysciences, Inc.; 2.0 μm diameter; 5.68 × 10^9 particles/mL) was added to 25 mL of the CTAB/NaSal solution, mixed, and then injected into the cross-slot device, which was placed on the stage of an Olympus IX-71 microscope (20× objective; NA = 0.40; magnification = 1.22 μm pixel^{-1}), which was focused to the midplane of the device, and frames were captured using a Redlake MotionXtra HG-100K high-speed camera. 625 frames (1504 pixels × 1128 pixels) were acquired at 100 frames s^{-1} (exposure time = 500 μs). Every 10th frame was used in the PIV analysis using Flow Manager software (Dantec Dynamics), making the effective frame rate 10 frames s^{-1}. An adaptive cross-correlation algorithm (with a low pass Gaussian filter) was applied to 64 × 64 pixel subunits of sequential frames to determine the local velocity vector $\underline{v}$. Finite element calculations of Stokes flow were also carried out (using Comsol Multiphysics 3.2, Comsol Inc.) to determine the relationship between volumetric flow rate and wall shear rate and to determine the effective channel height for calculation of birefringence.

III. Results

A. LVE of Wormlike Micellar Surfactant Solutions. We plot $G^*(\omega)$ data on the 30 mmol L^{-1} CTAB/240 mmol L^{-1} NaSal solution (Figure 1a), which, to the best of our knowledge, are unavailable elsewhere in the literature. We do note that Shikata et al. have studied the rheology of CTAB/NaSal systems in great detail[31,32] and pointed out that scission and fusion processes govern their stress relaxation, as also determined for other wormlike micellar fluids.[48] The fluid's plateau and terminal response regimes are clearly visible. Apart from the terminal G'' peak at $\omega \approx 1$ rad s^{-1}, another peak is visible in G'' at $\omega \approx 80$ rad s^{-1}. While the low ω peak signifies the terminal relaxation of the wormlike micellar chains at a time scale τ_T, the high-frequency peak clearly arises from faster relaxation modes. Note the slight decrease in G' with decreasing frequency and the high-frequency peak in the loss tangent tan δ also associated with the high-frequency relaxation.

For a single Maxwell element the following relations are well-known.

$$\frac{G(t)}{G_0} = \exp\left(-\frac{t}{\tau}\right)$$

$$\frac{G'(\omega)}{G_0} = \frac{\omega^2\tau^2}{1+\omega^2\tau^2}; \qquad \frac{G''(\omega)}{G_0} = \frac{\omega\tau}{1+\omega^2\tau^2} \tag{3}$$

$G(t)$ is the stress-relaxation modulus, τ is a relaxation time scale, and G_0 is a modulus scale. Although Maxwellian behavior is predicted by a quasi-network model, the limitations of this analysis have been discussed.[32] Moreover, the details of departure from Maxwellian behavior are instructive. Specifically, the terminal G'' peak is not single-exponential (see inset Figure 1b), as the data deviate from a Maxwell fit for $\omega \geq 2$ rad s^{-1}, signaling that micellar chain scission occurs on time scales that are not widely separated from terminal relaxation ($\tau_T \approx 0.91$ s). This deviation from Maxwellian behavior, which is also seen in other experimental data sets,[75−78] is nicely anticipated by Cates' tube model based theory of wormlike micellar fluid dynamics.[53,79,80] A Cole−Cole G'' vs G' plot (also called a "Han plot"[81]) is shown (Figure 1b). Scission processes cause deviation from the pure semicircle expected for pure Maxwellian relaxation, as seen in many wormlike micellar fluids.[75,77,82−84] We note that telechelic polymers may also exhibit near-Maxwellian relaxation, where the terminal time may similarly be significantly longer than the characteristic time of chain detachment and association.[85]

We further interpret these LVE data using the Granek−Cates (GC)[86,87] and Turner−Cates (TC)[80] theoretical models of stress relaxation in wormlike micelles as a basis. Since the Cole−Cole plot shows a linear asymptote with a slope ≈−1 as the well-defined minimum on the plot is approached (Figure 1b), we conclude in fidelity with the TC model that reptation is the dominant mechanism on the time scale of chain scission, τ_b, and that tube length fluctuations (breathing modes) do not dominate stress relaxation on the time scale τ_b. This conclusion gives $\tau_b \approx 0.5$ s. Also, since τ_b is comparable to τ_T, and our data clearly show that the dominant chain motion on the chemical time scale τ_b is by entangled (and certainly not unentangled) modes, we also infer in keeping with the GC *ansatz* that τ_b is large enough such that $\tau_b \gg \tau_e$, where τ_e is the relaxation time of an entanglement strand, the time scale at which the chain "feels" itself trapped in a tube. The frequency $\omega_e = \tau_e^{-1}$ marks the high-frequency end of the entanglement plateau, above which G'' and G' cross over such that $G'' > G'$ and enter the transition zone of LVE, and for this system $\omega_e >$ 100 rad s^{-1}, suggesting $\tau_e < 0.01$ s.

The steady shear and OS rheology of the 100 mmol L^{-1} CPyCl/60 mmol L^{-1} NaSal system have already been studied by Lee et al.[46] and are not repeated here. Their steady shear measurements[46] demonstrated the classical stress plateau seen in shear-banded fluids. Their LVE measurements at 25 °C show a clear terminal G'' peak, with $\tau_T = 2.5$ s, non-Maxwellian

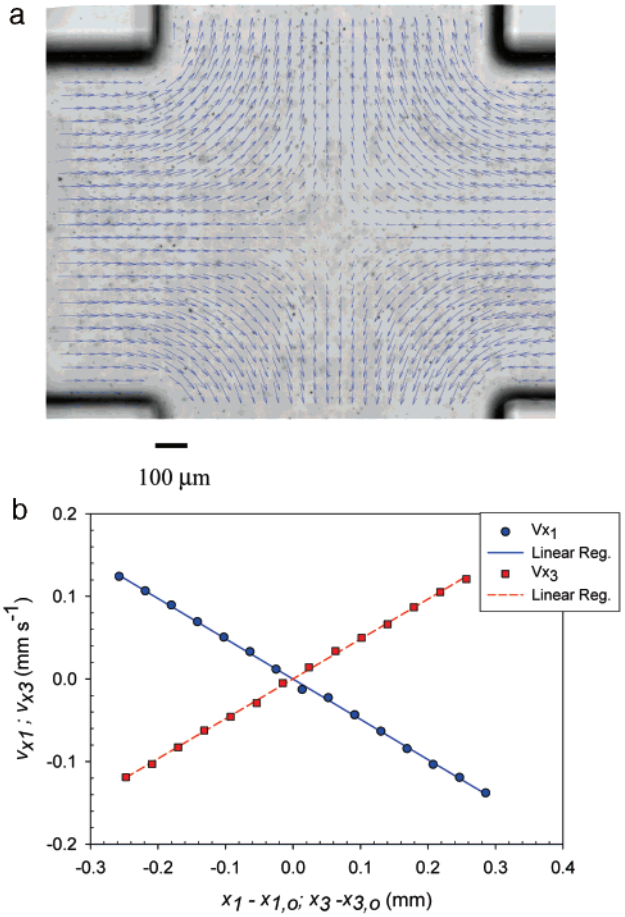

Figure 2. (a) μ-PIV: velocity vectors (denoted by arrows) in the middle focal plane of the cross-slot device for CTAB/NaSal solution flowing at $Q_{nom} = 0.25$ mL h^{-1}. (b). Strain rate $\dot{\epsilon}_0$ evaluated from μ-PIV data. Tracer particle velocity components in the 1 and 3 directions are plotted vs respective spatial coordinates. The SP's coordinates are ($x_{1,0}$, $x_{3,0}$). Discrete points and lines denote experimental data and linear regression fits to data (cf. eq 4), respectively. Standard uncertainty associated with velocity vector magnitudes is ± 10 μm s^{-1}.

relaxation (again consistent with reptation) at $\omega \geq 10$ rad s^{-1} (implying $\tau_b \approx 0.1$ s), and no higher frequency G'' peak (so that once again $\tau_b \gg \tau_e$).

B. μ-PIV. The μ-PIV results (Figure 2a) are shown as calculated velocity vectors superposed on a bright-field image of the channel with the seeded CTAB/NaSal solution flowing through it. The SP, where the velocity vanishes, is clearly visible in the middle of the channel. The midplane velocity profile agrees nicely with the definition of PEF:[88]

$$\underline{v} = \begin{pmatrix} -\dot{\epsilon}_0 x_1 \\ 0 \\ +\dot{\epsilon}_0 x_3 \end{pmatrix} \tag{4}$$

In a steady elongational flow the stretching rate $\dot{\epsilon}_0$ must be time-invariant. The μ-PIV data were analyzed by plotting $v_1(x_1 - x_{1,0})$ and $v_3(x_3 - x_{3,0})$, where ($x_{1,0}$, $x_{3,0}$) denote the SP coordinates in the (1,3) plane. Both v_1 and v_3 vanish at the SP, as expected (Figure 2b). Equation 4 predicts that these plots should be linear with slopes $-\dot{\epsilon}_0$ and $\dot{\epsilon}_0$, respectively. The least-squares linear regression to these data gives $\dot{\epsilon}_0(Q_{nom} = 0.25$ mL h$^{-1}) = 0.48$ s^{-1}. Q_{nom} is the nominal volume flow rate (and $\dot{\epsilon}_0 \sim Q_{nom}$), which is related to the total flow rate (for two inlets) $Q_{tot} = 2Q_{nom}$. Additional results of μ-PIV at higher flow rates will be discussed below. Although PEF is well approximated at the midplane, the extension rate decreases to zero approaching either the top or bottom surface of the channel. Since optical retardation arises from the integrated effect across the entire gap, the effective channel height is $h_{eff} = 0.50h$.

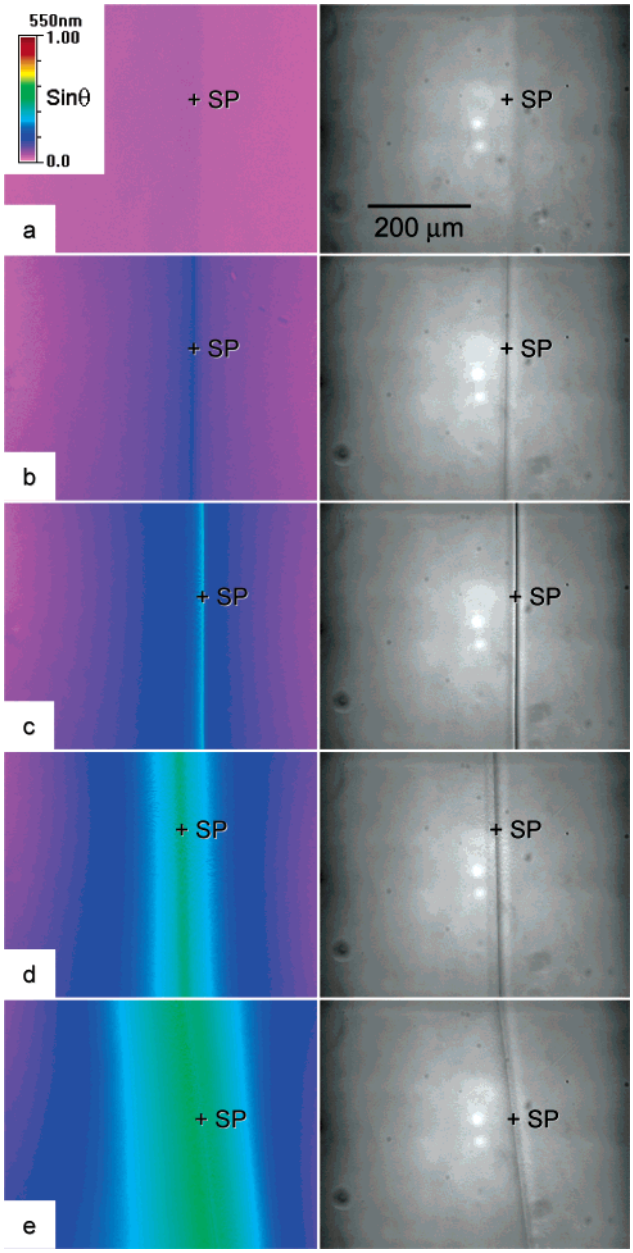

Figure 3. Sin θ profiles (in false colors) and transmitted light intensity images (in pairs; imaged in the mid-focal plane) for the 30 mmol L^{-1} CTAB/240 mmol L^{-1} NaSal solution at (a) $Q_{nom} = 0.1$ mL h^{-1}, (b) $Q_{nom} = 0.30$ mL h^{-1} (c) $Q_{nom} = 0.45$ mL h^{-1}, (d) $Q_{nom} = 0.7$ mL h^{-1}, and (e) $Q_{nom} = 0.8$ mL h^{-1}. The sin θ color code is shown in (a), and the stagnation point is marked "SP".

C. Birefringence, Banding, and the Stress−Optical Rule. Much of the FIB phenomenology exhibited by these fluids is illustrated in Figure 3, which shows images of the spatial variation of the background-subtracted sin θ (in false colors) and the corresponding transmitted light intensity (eq 2) from the CTAB/NaSal system. The fluid flows in along the 1 direction (from the left and right) and flows out along the 3 (stretching) direction (to the top and bottom). The principal axes of the stress tensor $\underline{\underline{T}}$ in PEF coincide with these directions due to flow symmetry.

$$\underline{\underline{T}} = \begin{pmatrix} T_{11} & 0 & 0 \\ 0 & T_{22} & 0 \\ 0 & 0 & T_{33} \end{pmatrix}_{123} \quad (5)$$

At Q_{nom} values between 0.05 and 0.25 mL h^{-1}, a broad increase of sin θ was seen near the SP. The magnitude of the peak sin θ increases with increasing Q_{nom}. A typical result in this flow rate range is shown in Figure 3a (Q_{nom} = 0.1 mL h^{-1}), where the flow is slow enough such that the SOR holds. Starting at Q_{nom} = 0.3 mL h^{-1} (Figure 3b), the peak in sin θ narrows somewhat, and a narrow sharp band becomes visible in the transmitted light intensity image. At still higher Q_{nom}, the transmitted light intensity contrast sharpens, and the sin θ peak grows markedly. This birefringence band reflects the increased alignment of wormlike micelles along the outflow direction. At Q_{nom} = 0.45 mL h^{-1} (Figure 3c) the birefringence inside the band becomes practically constant, reflecting quasi-saturation of alignment of wormlike micellar chains in the band, while the transmitted light intensity contrast grows further. Demonstrating that this contrast arises from low-angle scattering, we find that it vanishes when the NA is sufficiently large. At Q_{nom} = 0.70 mL h^{-1} (Figure 3d) the birefringence band had broadened further, along with a slight counterclockwise rotation of its principal axis. The band broadening occurred only after the saturation of the intensity in the middle of the band. Finally, at Q_{nom} = 0.80 mL h^{-1} (Figure 3e) the flow becomes markedly asymmetric, and the fluid flows out of the channel along a preferred direction. μ-PIV of these various flow rates demonstrates that neither the Δn nor the transmittance bands are shear bands; i.e., the rate of deformation remains uniform across the band (see Figure S1 in the Supporting Information). Even after the flow becomes asymmetric, no significant shear banding is observed. The data on the CPyCl/NaSal system are qualitatively similar, and the spatial variation of sin θ in this system is summarized in Figure 4.

There is striking similarity between these two fluids in the sin θ profiles during band formation. At low flow rates, the sin θ distribution width, quantified by the full-width at half-maximum (fwhm), is rather broad. As Q_{nom} is increased, the fwhm initially decreases (due to band formation) and decreases until sin θ reaches a plateau, after which it starts to increase again. Remarkably, the band observed in transmittance (e.g., Figure 3e) does not broaden when the birefringence band does. The fwhm and sin θ_{peak} (inside the band) are plotted vs the extensional Weissenberg number, $Wi_{ext} = \tau_T \dot{\epsilon}_0$, in Figure 5. A plateau in sin θ_{peak} and a distinct local minimum in the fwhm are seen in both systems, revealing that birefringence banding occurs in wormlike micelles undergoing PEF.

In Figure 6, we quantify the aforementioned asymmetry in terms of the angle Φ, a measure of how symmetric planar elongation becomes unstable since it is the tilt angle between the principal axis of the band along the outflow direction and the channel outflow axis. For a perfectly symmetric PEF, Φ = 0°. Clearly, the flow symmetry splits and the inlet streams are directed predominantly to either outlet channel as Wi_{ext} exceeds unity, suggesting that fluid elasticity effects are responsible. The phenomenon is neither inertial as Re is $O(10^{-4})$, nor is it slip-induced as there is no shear banding (see μ-PIV video in the Supporting Information). Instead, there is less elasticity associated with the asymmetric mode (approximately simple shearing) vis-à-vis symmetrical pure extension. The two wormlike fluids however do not obey the same $\Phi(Wi_{ext})$ scaling. In the CTAB/NaSal fluid $\Phi \sim \sqrt{Wi_{ext} - Wi_{ext,c}} = 15.1°\sqrt{Wi_{ext} - 1.24}$, but the CPyCl/NaSal fluid does not have a similar scaling, for reasons

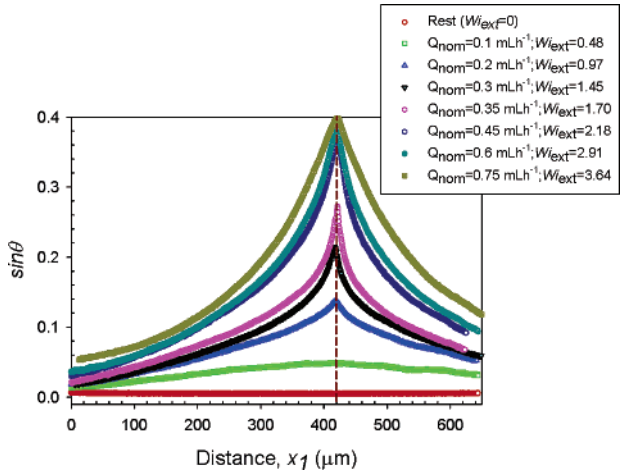

Figure 4. Sin θ vs spatial position x_1 in the 100 mmol L^{-1} CPyCl/60 mmol L^{-1} NaSal solution. Dashed lines denote SP coordinate in the 1 direction. Standard uncertainty in sin θ is ±0.004.

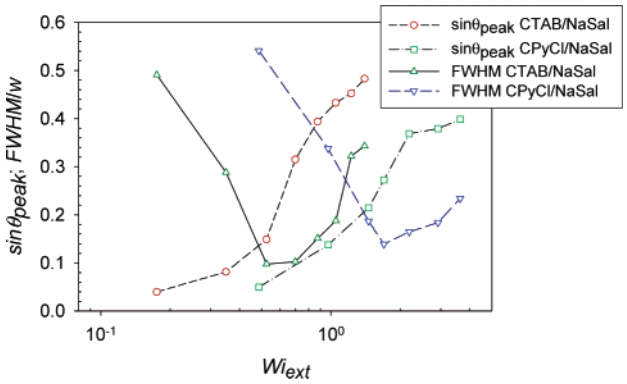

Figure 5. Full width at half-maximum (fwhm) of the sin θ distribution and peak sin θ values from Figures 3 and 4 plotted vs Wi_{ext}. Lines merely guide the eye.

that are currently unclear. Arratia et al.[89] have recently reported a similar flow instability in a dilute polyacrylamide (M_w = 18 × 10^6) solution where the velocity field becomes asymmetric above some critical strain rate in a cross-slot. We believe that this behavior is generic to elastic fluids and is not limited to wormlike micellar fluids or polymer solutions.

The relationship between the phase difference θ and the birefringence Δn is as follows.

$$\Delta n = \frac{\theta\lambda}{2\pi h_{eff}} \quad (6)$$

$\Gamma = \Delta n h_{eff}$ is the retardation, which causes the phase difference. Since light is sent down the 2 direction, the measured birefringence $\Delta n = n_3 - n_1$, where n_3 and n_1 denote the refractive indices in the 3 and 1 directions, respectively. A plot of the peak Δn vs Wi_{ext} is shown in Figure 7 for both the CTAB/NaSal and the CPyCl/NaSal systems. We discuss the CTAB/NaSal system first. For $Wi_{ext} < 0.40$, linear growth in Δn is seen with Wi_{ext}. As Wi_{ext} exceeds 0.4, the slope increases and the birefringence band forms. This regime of increased slope is followed by a narrow regime where Δn essentially saturates for $0.7 < Wi_{ext} < 1.0$. A further slight increase in Δn and a rotation of the principal axes at the SP follow at higher Wi_{ext}, indicative of the same flow instabilities discussed earlier (cf. Figure 6).[90] The CPyCl/NaSal system shows qualitatively similar behavior: linear growth at small Wi_{ext}, followed by deviation from linear growth, and finally by saturation. Linear regression

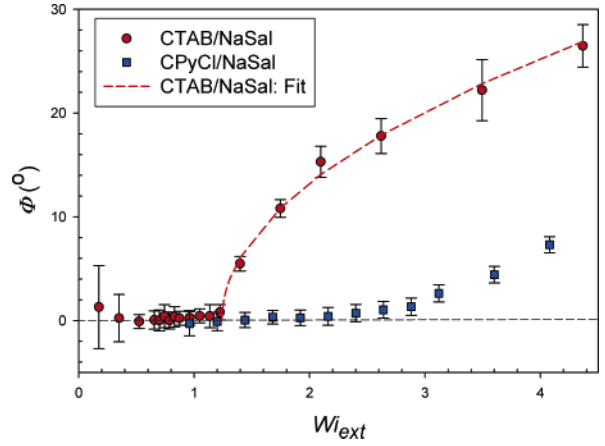

Figure 6. Tilt angle Φ vs Wi_{ext} for the 30 mmol L^{-1} CTAB/240 mmol L^{-1} NaSal and 100 mmol L^{-1} CPyCl/60 mmol L^{-1} NaSal solutions. The smooth curve indicates a fit to the CTAB/NaSal data (discussed in text). Bars on data points in all figures denote standard uncertainty associated with one standard deviation.

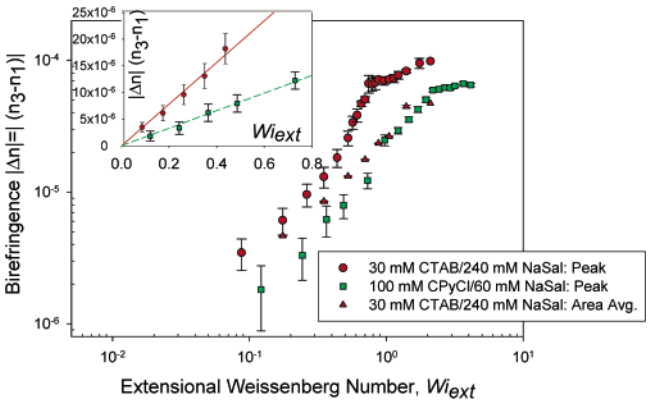

Figure 7. Birefringence Δn (from peak in sin θ in the birefringence band) vs Wi_{ext} for the 30 mmol L^{-1} CTAB/240 mmol L^{-1} NaSal and 100 mmol L^{-1} CPyCl/60 mmol L^{-1} NaSal solutions. The area-averaged birefringence of the CTAB/NaSal fluid is also plotted for comparison with peak values. The inset shows the peak Δn data (symbols) vs Wi_{ext} on linear scales; lines denote linear regression fits.

fits to the low Wi_{ext} data for both systems are shown in the inset of Figure 7. The slopes of the straight lines that pass through the origin (and hence signify correct background subtraction) are 3.9×10^{-5} and 1.6×10^{-5} for the CTAB/NaSal and the CPyCl/NaSal systems, respectively. Quite intriguingly, when the peak Δn is plotted vs a dimensionless breaking time ($= \tau_b \dot{\epsilon}_0$) for the two systems, the low strain rate data and high strain rate data seem to show similar limiting behavior for both systems (see Figure S2 in the Supporting Information). We believe that this result underscores the need for a deeper understanding of the physics underlying the breaking time scale.

Kato et al.,[63] who used an 800 μm spot size laser, have reported spatially averaged Δn values from their FRM experiments on a 30 mmol L^{-1} CTAB/230 mmol L^{-1} NaSal solution that are about a factor of 15 smaller than ours, as we report a local peak in the measured Δn value within the birefringence band, while their values are spatial averages over the extensional flow field. The [NaSal] in their system is 10 mmol L^{-1} smaller than ours, and their experiments are done at slightly lower temperatures (18−21 °C). While these effects also contribute to the differences in Δn, nevertheless the dominant contribution to the difference likely arises from spatial averaging. When the retardation is averaged in a 640 μm × 485 μm area near the SP, somewhat lower values of Δn are obtained (Figure 7).

The SOR[91] relates $\underline{\underline{T}}$ and the refractive index tensor $\underline{\underline{n}}$ in optically anisotropic media. When light is sent down a principal direction (taken here as the 2 direction), the SOR is stated thus.

$$\Delta n_{31} = n_3 - n_1 = C(T_{33} - T_{11}) \tag{7}$$

C denotes the stress−optical coefficient. The SOR provides a noninvasive measure of rheological material functions, if it holds for the fluid at the relevant deformation rates. The regime where both $T_{33} - T_{11}$ and Δn grow linearly with $\dot{\epsilon}_0$ is where the SOR is valid. For the CTAB/NaSal data, this regime is restricted to $0.0 < Wi_{ext} < 0.4$. For $Wi_{ext} > 0.4$ the linearity no longer holds in the Δn data while $T_{33} - T_{11}$ continues to grow linearly, leading to a natural failure of the SOR. For the CPyCl/NaSal system, this linearity holds up to $Wi_{ext} \cong 0.8$.

Having established the regime where the SOR holds for the CTAB/NaSal fluid, we can apply eq 7 (using $C = -5.74 \times 10^{-7}$ Pa^{-1} [50]) to determine its first planar elongational viscosity, $\eta_{p,1}$, and $T_{33} - T_{11}$.

$$\eta_{p,1}(\dot{\epsilon}_0) = -\frac{(T_{33} - T_{11})}{\dot{\epsilon}_0} \tag{8}$$

(A substantially different value of C was reported by Shikata et al.:[55] $C = -3.1 \times 10^{-7}$ Pa^{-1}.) For the Newtonian regime, we can expect $\eta_{p,1} = 4\eta_0$[88] in PEF, and our data recover this relationship within the bounds of appreciable experimental uncertainty. Given the large spread between the C's, we do not overemphasize the comparison of $\eta_{p,1}$ and zero shear viscosity, η_0 (= 10.5 Pa·s[63]).

D. Wall Shear. A critical concern in our experiments is the effect of wall shear on these FIB measurements under PEF, motivating the need to quantify wall shear effects alone. We accomplished this by measuring FIB of the CTAB/NaSal fluid in an inlet channel of the cross-slot device at different and higher Q_{nom}'s to get a good signal as the shear birefringence can be reasonably expected to be much weaker than that from pure straining flow. The sin θ image for wall-induced shear is shown in the inset of Figure 8. The side wall lies at the bottom of this image, and fluid flows from right to left. Because of wall shear, the micelles are locally aligned and birefringence develops. Note that the micellar orientation here is perpendicular to the orientation at the SP. The shear birefringence Δn_{shear} far from the side walls was measured and plotted in Figure 8 along with the extensional birefringence Δn_{PEF} as a function of the characteristic Weissenberg numbers $Wi_{shear} = \tau_T \dot{\gamma}$ ($\dot{\gamma} = 8Q_{nom}/wh^2$) and Wi_{ext}, respectively. The prefactor 8.0 was determined from finite element calculations for the prescribed channel geometry and dimensions. Similar to Δn_{PEF}, Δn_{shear} also saturates, but at larger $Wi_{shear} \geq 10$. The Δn_{PEF} grows with a larger slope and also saturates faster than Δn_{shear}, as expected. The slopes (in the linear regime) for Δn_{PEF} and Δn_{shear} are 3.9×10^{-5} and 3.1×10^{-6}, respectively. The distinctly larger slope in Δn_{PEF} demonstrates the efficacy of extensional flows in stretching and aligning fluid elements. When compared at numerically equal $Wi_{ext} = Wi_{shear}$, Δn_{shear} is more than a factor of 10 smaller than Δn_{PEF}. While wall shear undoubtedly contributes to the fluid's deformation history (and hence to the retardation that is sampled throughout the channel depth), it is simply overwhelmed by the dominant PEF contribution.

E. Birefringence Relaxation. The extensional deformation experienced by the fluid weakens as it enters the outlet channels. To study the spatiotemporal decay of Δn for the CTAB/NaSal fluid along the centerline of the outflow axis with increasing distance from the SP, the retardation Γ was measured in two

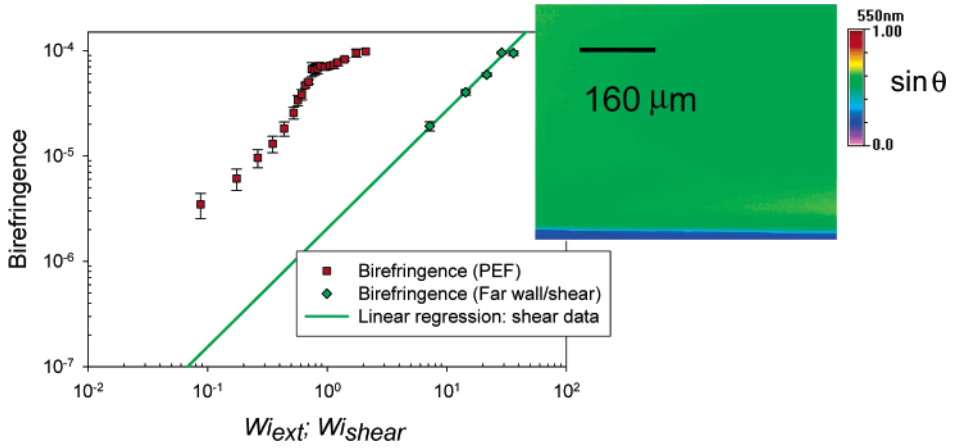

Figure 8. Comparison of peak birefringence (inside the band) from PEF and far-wall birefringence from shear for the 30 mmol L^{-1} CTAB/240 mmol L^{-1} NaSal solution, plotted vs Wi_{ext} and Wi_{shear}, respectively. Inset: birefringence arising from shear at the wall in the 30 mmol L^{-1} CTAB/240 mmol L^{-1} NaSal solution at $Q_{nom} = 5.0$ mL h^{-1}.

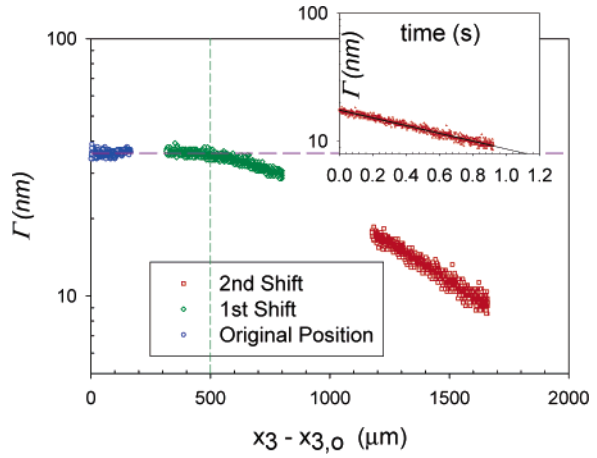

Figure 9. Retardation Γ (nm) vs spatial distance $x_3 - x_{3,0}$ from the SP along outflow (3) direction for the 30 mmol L^{-1} CTAB/240 NaSal solution at $Q_{nom} = 0.5$ mL h^{-1} ($Wi_{ext} = 0.87$). Inset: Γ (shear contribution deducted) vs time for the fluid using data from the second shifted position of the device (fluid inside outlet channel). Standard uncertainty in Γ is ±1 nm.

other locations—one near the entrance of one of the outlets and the other much further into that outlet channel (Figure 9). Γ starts to exponentially decay from its constant level in the extensional flow field at $x_3 - x_{3,0} \approx 500$ μm, where the fluid leaves the extensional flow field by entering the outlet channel. (The shear contribution to birefringence in the outlet channel was subtracted here to focus solely on PEF alignment effects.) The inset to Figure 9 shows the temporal decay of Γ, measured at the second shifted position of the device with time being counted starting when the fluid entered that frame. From linear regression, the observed birefringence relaxation time scale is 1.4 s, close to the fluid's longest relaxation time (0.91 s), as expected.

IV. Discussion

A. Time Scales and Equilibrium Micellar Length Distribution. To place fundamental time scales and rate constants in this problem in perspective to rationalize our birefringence results, we apply the GC model further[86,87] to our data. We determine the chain scission constant k_{sciss} from Cates' prediction,[79] which says that the longer the chain, the larger its probability to experience stochastic scission: $k_{sciss} = 1/\tau_b\langle l\rangle$. In the CTAB/NaSal fluid, $\tau_b = 0.5$ s and average contour length $\langle l\rangle \approx 4.6$ μm (see Appendix for $\langle l\rangle$ calculation), so that $k_{sciss} = 4 \times 10^5$ m^{-1} s^{-1}. The equilibrium distribution $f_0(l)$ of instantaneous micellar chain lengths is exponential.[86]

$$f_0(l) = \langle l\rangle^{-2} \exp\left(-\frac{l}{\langle l\rangle}\right)$$

$$\langle l\rangle = \sqrt{\frac{k_{sciss}}{2k_{fus}}} \qquad (9)$$

The fusion rate constant (k_{fus}) was evaluated using the $\langle l\rangle$; $k_{fus} = 1 \times 10^{16}$ m^{-3} s^{-1}. Using eq 9, $f_0(l)$ can also be determined. For the CPyCl/NaSal system, $\langle l\rangle \approx 8.2$ μm, $k_{sciss} = 1.2 \times 10^5$ m^{-1} s^{-1}, and $k_{fus} = 9 \times 10^{15}$ m^{-3} s^{-1}. Since k_{fus} reflects molecular dynamics, its similarity for the two systems is expected. Somewhat more significant differences in k_{sciss} reflect differences in the free energy of association. We have thus estimated the equilibrium distribution, rate constants, and fundamental rheological time scales of these fluids.

Another time scale, which is independent of fluid properties, but dependent on channel geometry, flow rate, and spatial position, is the residence time, τ_{res}

$$\tau_{res} \approx \frac{1}{\dot{\epsilon}_0} \ln\left(\frac{x_{1,i}}{x_1}\right) \qquad (10)$$

where $x_{1,i}$ locates the onset of extensional flow (approximately $w/2$). We replot the data of Figures 3 and 4 as sin $\theta(\epsilon)$, where the strain ϵ was calculated as $\epsilon = \tau_{res}\dot{\epsilon}_0$ (Figure 10a,b). At each flow rate, the fluid has sufficient time to let the micellar chains disentangle near the SP, causing a high degree of alignment and the formation of birefringence bands. Given the strong flow field and that $Wi_{ext} \rightarrow 1$, we can safely expect convective constraint release (CCR) effects[92−100] to be operational here. Milner et al. have applied their microscopic CCR model[99] to predict[100] shear bands in micelles in shear flows where $Wi_{shear} \geq 1$.

B. Birefringence Bands and Transmittance Bands. Our data indicate that birefringence bands and transmittance bands have distinct features. Particularly at high flow rates, the width of these bands can be significantly different (e.g., in Figure 3e). These high rates (and stress) cause a high degree of alignment (birefringence) over a broad area in the cross-slot. However, when the flow is asymmetric, the fluid experiences nearly simple shear. Interestingly, this change in flow type is not accompanied by significant shear banding, suggesting that the effective viscosity is nearly uniform (see μ-PIV videos in Supporting

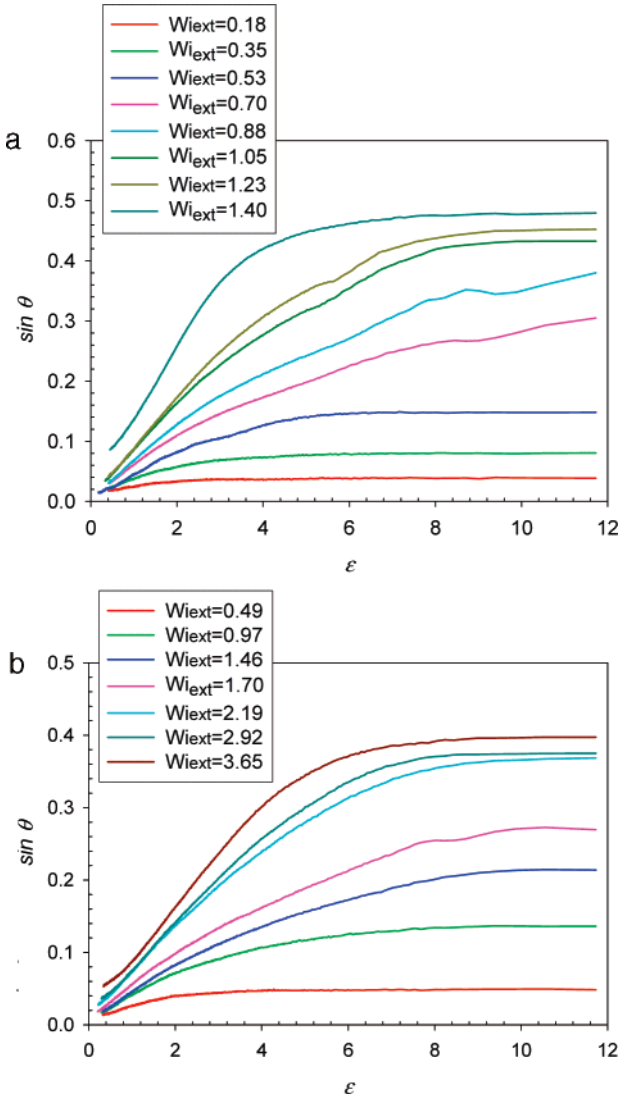

Figure 10. Sin θ plotted vs strain ϵ for (a) 30 mmol L^{-1} CTAB/240 mmol L^{-1} NaSal solution and (b) 100 mmol L^{-1} CPyCl/60 mmol L^{-1} NaSal solution (Figure 4 caption has uncertainty information).

Information). In this respect, our results sharply contrast the conclusions of Drappier et al.,[52] who have recently used a combination of flow birefringence and flow velocimetry by magnetic resonance imaging (MRI) in a 69 mmol L^{-1} CTAB/25 mmol L^{-1} NaSal solution undergoing simple shear in a Couette cell. However, the shear rate is not uniform when the Couette gap is large. Although their birefringence experiments were done in a narrow gap (1 mm) Couette cell, the MRI experiments were done in a wide gap Couette cell (1 cm). They have quantitatively compared the proportion of the shear-induced phase in the shear band and the birefringent band and reached the conclusion that they are exactly correlated, after ignoring a second birefringent band close to the outer wall by calling it an experimental artifact. In a wide gap Couette cell, the imposed shear rate (in a rate controlled instrument) does not remain constant as it would in a narrow gap cell. Shear banding is extremely sensitive to the deformation rate and is best studied in narrow gap Couette cells wherein the shear rate will be practically constant across the gap.[101]

Our experiments also show that the band is subject to positional fluctuations (cf. results of Britton and Callaghan[102]). Our experiments on the CTAB/NaSal fluid show that the band suffers excursions in the 1 direction by $\approx$30 μm in the 1−3 plane (Figure 11). The Fourier transform in Figure 11 shows

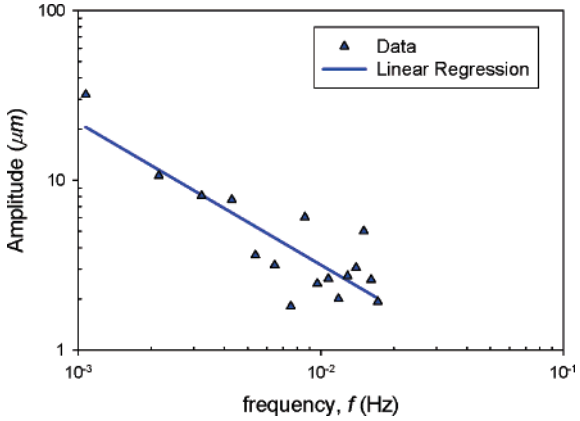

Figure 11. Fourier transform of the fluctuations of the spatial position of the birefringence band in the 30 mmol L^{-1} CTAB/240 mmol L^{-1} NaSal system. Standard uncertainty in amplitude is ± 1 μm.

that the amplitude of the fluctuations in band position scales approximately as f^{-1}, where f denotes frequency, suggesting random fluctuations. This movement was much more pronounced in the CTAB/NaSal fluid than in the CPyCl/NaSal fluid due to smaller viscosity in the former system. At high flow rates, well above the transition to asymmetric flow, positional fluctuations are very rapid, and the angle Φ also fluctuates from positive to negative values, in agreement with the results of Arratia et al.[89]

While the birefringence bands and transmittance bands are qualitatively similar in the CTAB/NaSal and CPyCl/NaSal systems, Figure 7 reveals quantitative differences between the scaling of their Δn with Wi_{ext}, apart from the differences in the slopes in the smallest Wi_{ext} regime. The Δn in the CTAB/NaSal system saturates at $Wi_{ext} = 0.7$, while it saturates at $Wi_{ext} = 2$ in the CPyCl/NaSal system. What causes this marked difference in the deformation required to reach saturation? While we suggest that the saturated Δn is indicative of (nearly) fully extended and aligned chains, we argue that the micellar breakup kinetics, which is markedly different in the two fluids, may cause this difference. Since $\tau_b/\tau_T \approx 0.5$ in the CTAB/NaSal system, the average micellar length in that system is shorter compared to that in the CPyCl/NaSal system, where τ_b is comparatively $\ll \tau_T$ ($\tau_b/\tau_T \approx 0.04$). Differences are also likely in the hydrodynamic force required to pull a chain to its fully stretched state, which is of order $f_{hydro} = \eta_s \langle l \rangle^2 \dot{\epsilon}_0$,[103] where η_s denotes solvent viscosity. In both systems the asymptotic birefringence is $\approx 7 \times 10^{-5}$, suggesting that the asymptotic chain conformations reflect similar (near-) complete alignment of micellar chains. The longer CPyCl/NaSal micellar chains thus show a birefringence asymptote at higher Wi_{ext}.

The transmittance band (e.g., Figure 3c) is aligned with the outflow direction and intersects the SP. When adjusting the focus through the gap, this band appears sharp over a span (in the 2 direction) of more than 300 μm, when $Q_{nom} = 0.55$ mL h^{-1} (i.e., the band does not span the entire channel depth). The fluid inside the band, which is separated from the surrounding fluid by a fairly sharp interface, does not represent a true equilibrium thermodynamic phase, as the interfaces merely signify the markedly different optical properties of the fluid within and outside the band. Since the birefringence and transmittance bands disappear upon flow cessation, they have hydrodynamic (or nonequilibrium thermodynamic) origins. The wormlike micellar chains inside the band are highly aligned. The static evidence from flow-light scattering experiments of Kadoma and van Egmond[104,105] supports this physical picture. Upon shear

cessation, they saw the ubiquitous butterfly pattern,[106−108] reflecting the breakup of the aligned stringlike structures.

V. Conclusions

In conclusion, we have established the existence of birefringence and transmittance bands in wormlike micellar fluids in planar elongational flow. The mechanism of birefringence banding reveals similarity in the retardation profile measured across the birefringence band's width. The width of this retardation distribution initially decreases until the transmittance band is formed and then increases. The fluid inside the band has significantly different optical properties than the fluid outside the band. Using linear viscoelasticity data on the CTAB/NaSal fluid, we have quantified the fundamental rheological time scales and argued that in the regime (wherein our data lie), where the calculated residence time of the fluid in the extensional flow field exceeds the longest relaxation time of the micellar chains, the chains have sufficient time to be stretched and aligned with the field, enabling micellar chain alignment within the band. As the extensional flow weakens downstream of the stagnation point, the birefringence decays exponentially. The stress−optical rule fails at smaller extensional Weissenberg number than shear Weissenberg numbers, and it should certainly not be applied in an ad hoc fashion in these strong flows. At the highest Weissenberg numbers attained, the flow became asymmetric, but no shear banding was observed as the velocity profiles remained continuous in the asymmetric flow regime.

Acknowledgment. We thank David Boger, Fred Phelan, Alex Norman, Ralph Colby, and Norman Wagner for helpful discussions and suggestions at different stages of this work.

Appendix. Calculation of Average Contour Length

Granek and Cates[86] have predicted that in the limit $\tau_b \gg \tau_e$ (satisfied by our CTAB/NaSal data and also by the CPyCl/NaSal data of Lee et al.[46]) the average chain length ($\langle l \rangle$) is related to the entanglement strand length, l_e, in wormlike micellar fluids.

$$\frac{l_e}{\langle l \rangle} \approx \frac{G''_{min}}{G_N^\circ} \tag{A1}$$

G''_{min} is the dip value of G'' at the high ω end of the Cole−Cole plot, and G_N° is the plateau modulus, calculated from the area under the terminal G'' peak. From the CTAB/NaSal data we get $G''_{min} = 1.1$ Pa and $G_N^\circ \cong 8.2$ Pa, and from eq A1 we get $l_e/\langle l \rangle \approx 0.13$.

l_e can be estimated from G_N° using the following well-known relationship for entangled polymer solutions.[109]

$$G_N^\circ = \frac{k_B T \varphi}{v_e} \tag{A2}$$

k_B is Boltzmann's constant, T is absolute temperature, ϕ is polymer volume fraction, and v_e is the volume of polymer per entanglement strand.[109−111]

$$v_e \approx \pi R^2 l_e \tag{A3}$$

R is the micelle radius, taken as 2 nm here. Thus, l_e and $\langle l \rangle$ approximately equal 600 nm and 4.6 μm, respectively, in our CTAB/NaSal system. Similarly, for the CPyCl/NaSal fluid, using $G''_{min} = 1.8$ Pa and $G_N^\circ \cong 30$ Pa, we get $l_e \cong 500$ nm and $\langle l \rangle \cong 8.2$ μm. The micellar chains in the CPyCl/NaSal system are thus nearly twice as long as those in the CTAB/NaSal system. We note that the $\langle l \rangle$ values obtained by this method are approximate lower bounds,[86] especially at high salt concentrations for CTAB/KBr systems[83] and CTAC/NaSal/NaCl systems.[86]

Supporting Information Available: Two video files of μ-PIV data on the CTAB/NaSal fluid: At $Q_{nom} = 1.5$ mL h^{-1} (file name: piv qnom 1_f.avi) the video demonstrates that the flow is nearly linear near the stagnation point. The red line in this video merely guides the eye and connects two seed particles. This is a time-lapsed video, slowed down from real time by a factor of 50. The total elapsed real time between the beginning and the end of the video is 200 ms. The second video file (file name piv qnom 0_25c.avi) on the CTAB/NaSal fluid demonstrates planar elongation with a well-defined stagnation point at $Q_{nom} = 0.25$ mL h^{-1}. This video file is in real time. Additionally, we are submitting a variant of Figure 7 as Supporting Information, wherein Δn is plotted vs a dimensionless breaking time ($= \tau_b \dot{\epsilon}_0$) for the two wormlike micellar fluids. The velocity profile remains continuous in the asymmetric flow regime, and the continuous velocity profiles of the CTAB/NaSal fluid in the asymmetric regime are shown in Supporting Information. This material is available free of charge via the Internet at http://pubs.acs.org.

References and Notes

(1) Taylor, G. I. The Viscosity of a Fluid Containing Small Drops of Another Fluid. *Proc. R. Soc. London A* **1932**, *138*, 41−48.
(2) Taylor, G. I. The Formation of Emulsions in Definable Fields of Flow. *Proc. R. Soc. London A* **1934**, *146*, 501−523.
(3) Bentley, B. J.; Leal, L. G. An Experimental Investigation of Drop Deformation and Breakup in Steady Two-Dimensional Linear Flows. *J. Fluid Mech.* **1986**, *167*, 241−283.
(4) Stone, H. A.; Bentley, B. J.; Leal, L. G. An Experimental Study of Transient Effects in the Breakup of Viscous Drops. *J. Fluid Mech.* **1986**, *173*, 131−158.
(5) Keller, A.; Odell, J. A. The Extensibility of Macromolecules in Solution−A New Focus for Macromolecular Science. *Colloid Polym. Sci.* **1985**, *263*, 181−201.
(6) Muller, A. J.; Odell, J. A.; Keller, A. Polymer Degradation in Extensional Flow. *Polym. Commun.* **1989**, *30*, 298−301.
(7) Narh, K. A.; Odell, J. A.; Muller, A. J.; Keller, A. Polymer-Solution Degradation−the Combined Effects of Flow and Temperature. *Polym. Commun.* **1990**, *31*, 2−5.
(8) Odell, J. A.; Muller, A. J.; Narh, K. A.; Keller, A. Degradation of Polymer-Solutions in Extensional Flows. *Macromolecules* **1990**, *23*, 3092−3103.
(9) Odell, J. A.; Keller, A.; Rabin, Y. Flow-Induced Scission of Isolated Macromolecules. *J. Chem. Phys.* **1988**, *88*, 4022−4028.
(10) Odell, J. A.; Keller, A.; Miles, M. J. A Method for Studying Flow-Induced Polymer Degradation−Verification of Chain Halving. *Polym. Commun.* **1983**, *24*, 7−10.
(11) Islam, M. T.; Vanapalli, S. A.; Solomon, M. J. Inertial effects on polymer chain scission in planar elongational cross-slot flow. *Macromolecules* **2004**, *37*, 1023−1030.
(12) Kim, K.; Islam, M. T.; Shen, X.; Sirviente, A. I.; Solomon, M. J. Effect of macromolecular polymer structures on drag reduction in a turbulent channel flow. *Phys. Fluids* **2004**, *16*, 4150−4162.
(13) Vanapalli, S. A.; Islam, M. T.; Solomon, M. J. Scission-induced bounds on maximum polymer drag reduction in turbulent flow. *Phys. Fluids* **2005**, *17*, 095108.
(14) Schroeder, C. M.; Babcock, H. P.; Shaqfeh, E. S. G.; Chu, S. Observation of polymer conformation hysteresis in extensional flow. *Science* **2003**, *301*, 1515−1519.
(15) deGennes, P. G. Coil-Stretch Transition of Dilute Flexible Polymers under Ultra-High Velocity Gradients. *J. Chem. Phys.* **1974**, *60*, 5030−5042.
(16) Hudson, S. D.; Phelan, F. R.; Handler, M. D.; Cabral, J. T.; Migler, K. B.; Amis, E. J. Microfluidic analog of the four-roll mill. *Appl. Phys. Lett.* **2004**, *85*, 335−337.
(17) Astarita, G. Objective and Generally Applicable Criteria for Flow Classification. *J. Non-Newtonian Fluid Mech.* **1979**, *6*, 69−76.
(18) Batchelor, G. K. *An Introduction to Fluid Dynamics;* Cambridge University Press: Cambridge, 1974.
(19) Nguyen, T. Q., Kausch, H.-H., Eds. *Flexible Polymer Chains in Elongational Flow: Theory and Experiment;* Springer: Berlin, 1999.
(20) Janeschitz-Kriegl, H. *Polymer Melt Rheology and Flow Birefringence;* Springer-Verlag: Berlin, 1983.

(21) Fuller, G. G. *Optical Rheometry of Complex Fluids;* Oxford University Press: New York, 1995.
(22) Stone, H. A.; Kim, S. Microfluidics: Basic Issues, Applications and Challenges. *AIChE J.* **2001**, *47*, 1250−1254.
(23) Stone, H. A.; Stroock, A. D.; Ajdari, A. Engineering Flows in Small Devices: Microfluidics Toward a Lab-on-a-Chip. *Annu. Rev. Fluid Mech.* **2004**, *36*, 381−411.
(24) Cooper McDonald, J.; Duffy, D. C.; Anderson, J. R.; Chiu, D. T.; Wu, H.; Schueller, O. J. A.; Whitesides, G. M. Fabrication of Microfluidic Systems in Poly(dimethylsiloxane). *Electrophoresis* **2000**, *21*, 27−40.
(25) Whitesides, G. M.; Stroock, A. D. Flexible Methods for Microfluidics. *Phys. Today* **2001** (June), 42−48.
(26) Cabral, J. T.; Hudson, S. D.; Harrison, C.; Douglas, J. F. Frontal photopolymerization for microfluidic applications. *Langmuir* **2004**, *20*, 10020−10029.
(27) Bird, R. B.; Armstrong, R. C.; Hassager, O. *Dynamics of Polymeric Liquids: Fluid Mechanics*, 2nd ed.; John Wiley and Sons: New York, 1987; Vol. 1.
(28) Rodd, L. E.; Scott, T. P.; Boger, D. V.; Cooper-White, J. J.; McKinley, G. H. The inertio-elastic planar entry flow of low-viscosity elastic fluids in micro-fabricated geometries. *J. Non-Newtonian Fluid Mech.* **2005**, *129*, 1−22.
(29) Rehage, H.; Hoffmann, H. Rheological Properties of Viscoelastic Surfactant Systems. *J. Phys. Chem.* **1988**, *92*, 4712−4719.
(30) Rehage, H.; Hoffmann, H. Viscoelastic Surfactant Solutions—Model Systems for Rheological Research. *Mol. Phys.* **1991**, *74*, 933−973.
(31) Shikata, T.; Hirata, H.; Kotaka, T. Micelle Formation of Detergent Molecules in Aqueous-Media—Viscoelastic Properties of Aqueous Cetyltrimethylammonium Bromide Solutions. *Langmuir* **1987**, *3*, 1081−1086.
(32) Shikata, T.; Hirata, H.; Kotaka, T. Micelle Formation of Detergent Molecules in Aqueous-Media. 2. Role of Free Salicylate Ions on Viscoelastic Properties of Aqueous Cetyltrimethylammonium Bromide Sodium-Salicylate Solutions. *Langmuir* **1988**, *4*, 354−359.
(33) Makhloufi, R.; Decruppe, J. P.; Ait-Ali, A.; Cressely, R. Rheooptical Study of Worm-Like Micelles Undergoing A Shear Banding Flow. *Europhys. Lett.* **1995**, *32*, 253−258.
(34) Mair, R. W.; Callaghan, P. T. Observation of shear banding in worm-like micelles by NMR velocity imaging. *Europhys. Lett.* **1996**, *36*, 719−724.
(35) Cappelaere, E.; Cressely, R. Shear banding structure in viscoelastic micellar solutions. *Colloid Polym. Sci.* **1997**, *275*, 407−418.
(36) Lerouge, S.; Decruppe, J. P.; Humbert, C. Shear banding in a micellar solution under transient flow. *Phys. Rev. Lett.* **1998**, *81*, 5457−5460.
(37) Britton, M. M.; Mair, R. W.; Lambert, R. K.; Callaghan, P. T. Transition to shear banding in pipe and Couette flow of wormlike micellar solutions. *J. Rheol.* **1999**, *43*, 897−909.
(38) Bautista, F.; Soltero, J. F. A.; Perez-Lopez, J. H.; Puig, J. E.; Manero, O. On the shear banding flow of elongated micellar solutions. *J. Non-Newtonian Fluid Mech.* **2000**, *94*, 57−66.
(39) Lerouge, S.; Decruppe, J. P.; Berret, J. F. Correlations between rheological and optical properties of a micellar solution under shear banding flow. *Langmuir* **2000**, *16*, 6464−6474.
(40) Fischer, E.; Callaghan, P. T. Shear banding and the isotropic-to-nematic transition in wormlike micelles. *Phys. Rev. E* **2001**, *6401*.
(41) Decruppe, J. P.; Lerouge, S.; Berret, J. F. Insight in shear banding under transient flow. *Phys. Rev. E* **2001**, *6302*.
(42) Fischer, P.; Wheeler, E. K.; Fuller, G. G. Shear-banding structure orientated in the vorticity direction observed for equimolar micellar solution. *Rheol. Acta* **2002**, *41*, 35−44.
(43) Fielding, S. M.; Olmsted, P. D. Kinetics of the shear banding instability in startup flows. *Phys. Rev. E* **2003**, *68*, 036313.
(44) Lerouge, S.; Decruppe, J. P.; Olmsted, P. Birefringence banding in a micellar solution or the complexity of heterogeneous flows. *Langmuir* **2004**, *20*, 11355−11365.
(45) Hu, Y. T.; Lips, A. Kinetics and mechanism of shear banding in an entangled micellar solution. *J. Rheol.* **2005**, *49*, 1001−1027.
(46) Lee, J. Y.; Fuller, G. G.; Hudson, N. E.; Yuan, X. F. Investigation of shear-banding structure in wormlike micellar solution by point-wise flow-induced birefringence measurements. *J. Rheol.* **2005**, *49*, 537−550.
(47) Janeschitz-Kriegl, H.; Papenhuijzen, J. M. P. Flow birefringence in concentrated detergent solutions. *Rheol. Acta* **1971**, *10*, 461−466.
(48) Wunderlich, I.; Hoffmann, H.; Rehage, H. Flow Birefringence and Rheological Measurements on Shear Induced Micellar Structures. *Rheol. Acta* **1987**, *26*, 532−542.
(49) Cappelaere, E.; Berret, J. F.; Decruppe, J. P.; Cressely, R.; Lindner, P. Rheology, birefringence, and small-angle neutron scattering in a charged micellar system: Evidence of a shear-induced phase transition. *Phys. Rev. E* **1997**, *56*, 1869−1878.
(50) Humbert, C.; Decruppe, J. P. Flow birefringence and stress optical law of viscoelastic solutions of cationic surfactants and sodium salicylate. *Eur. Phys. J. B* **1998**, *6*, 511−518.
(51) Decruppe, J. P.; Ponton, A. Flow birefringence, stress optical rule and rheology of four micellar solutions with the same low shear viscosity. *Eur. Phys. J. E* **2003**, *10*, 201−207.
(52) Drappier, J.; Bonn, D.; Meunier, J.; Lerouge, S.; Decruppe, J. P.; Bertrand, F. Correlation between birefringent bands and shear bands in surfactant solutions. *J. Stat. Mech.*, 2006, P04003.
(53) Cates, M. E. Nonlinear Viscoelasticity of Wormlike Micelles (and Other Reversibly Breakable Polymers). *J. Phys. Chem.* **1990**, *94*, 371−375.
(54) Spenley, N. A.; Cates, M. E.; Mcleish, T. C. B. Nonlinear Rheology of Wormlike Micelles. *Phys. Rev. Lett.* **1993**, *71*, 939−942.
(55) Shikata, T.; Dahman, S. J.; Pearson, D. S. Rheooptical Behavior of Wormlike Micelles. *Langmuir* **1994**, *10*, 3470−3476.
(56) Humbert, C.; Decruppe, J. P. Stress optical coefficient of viscoelastic solutions of cetyltrimethylammonium bromide and potassium bromide. *Colloid Polym. Sci.* **1998**, *276*, 160−168.
(57) Chen, C. M.; Warr, G. G. Light scattering from wormlike micelles in an elongational field. *Langmuir* **1997**, *13*, 1374−1376.
(58) Hu, Y.; Wang, S. Q.; Jamieson, A. M. Elongational Flow Behavior of Cetyltrimethylammonium Bromide Sodium-Salicylate Surfactant Solutions. *J. Phys. Chem.* **1994**, *98*, 8555−8559.
(59) Prudhomme, R. K.; Warr, G. G. Elongational Flow of Solutions of Rodlike Micelles. *Langmuir* **1994**, *10*, 3419−3426.
(60) Walker, L. M.; Moldenaers, P.; Berret, J. F. Macroscopic response of wormlike micelles to elongational flow. *Langmuir* **1996**, *12*, 6309−6314.
(61) Yesilata, B.; Clasen, C.; McKinley, G. H. Nonlinear shear and extensional flow dynamics of wormlike surfactant solutions. *J. Non-Newtonian Fluid Mech.* **2006**, *133*, 73−90.
(62) McKinley, G. H.; Sridhar, T. Filament-stretching rheometry of complex fluids. *Annu. Rev. Fluid Mech.* **2002**, *34*, 375−415.
(63) Kato, M.; Takahashi, T.; Shirakashi, M. Steady Planar Elongational Viscosity of CTAB/NaSal Solutions Measured in a 4-Roll Mill Flow Cell. *Nihon Reoroji Gakkaishi* **2002**, *30*, 283−287.
(64) Takahashi, T.; Yako, N.; Shirakashi, M. Relationship between shear-induced structure and optical anisotropy on CPyCl/NaSaI aqueous solution. *Nihon Reoroji Gakkaishi* **2001**, *29*, 27−32.
(65) Lodge, A. S. A Network Theory of Flow Birefringence and Stress in Concentrated Polymer Solutions. *Trans. Faraday Soc.* **1956**, *52*, 120−130.
(66) Cathey, C. A.; Fuller, G. G. The Optical and Mechanical Response of Flexible Polymer-Solutions to Extensional Flow. *J. Non-Newtonian Fluid Mech.* **1990**, *34*, 63−88.
(67) Talbott, W. H.; Goddard, J. D. Streaming Birefringence in Extensional Flow of Polymer-Solutions. *Rheol. Acta* **1979**, *18*, 505−517.
(68) Penfold, J.; Staples, E.; Tucker, I.; Carroll, P.; Clayton, I.; Cowan, J. S.; Lawton, G.; Amin, S.; Ferrante, A.; Ruddock, N. Elongational Flow Induced Ordering in Surfactant Micelles and Mesophases. *J. Phys. Chem. B* **2006**, *110*, 1073−1082.
(69) Cabral, J. T.; Hudson, S. D. Microfluidic approach for rapid multicomponent interfacial tensiometry. *Lab Chip* **2006**, *6*, 427−436.
(70) Certain commercial materials and equipment are identified in this paper in order to adequately specify the experimental procedure. In no case does such identification imply recommendation or endorsement by the National Institute of Standards and Technology, nor does it imply that these are necessarily the best available for the purpose.
(71) Kadoma, I. A.; van Egmond, J. W. "Tuliplike" scattering patterns in wormlike micelles under shear flow. *Phys. Rev. Lett.* **1996**, *76*, 4432−4435.
(72) Wood, I. G.; Glazer, A. M. Ferroelastic Phase Transition in BiVO4: Birefringence Measurements Using The Rotating Analyzer Methodol. *J. Appl. Crystallogr.* **1980**, *13*, 217−223.
(73) Adrian, R. J. Particle-Imaging Techniques for Experimental Fluid-Mechanics. *Annu. Rev. Fluid Mech.* **1991**, *23*, 261−304.
(74) Adrian, R. J. Twenty years of particle image velocimetry. *Exp. Fluids* **2005**, *39*, 159−169.
(75) Berret, J. F.; Appell, J.; Porte, G. Linear Rheology of Entangled Wormlike Micelles. *Langmuir* **1993**, *9*, 2851−2854.
(76) Candau, S. J.; Hirsch, E.; Zana, R.; Delsanti, M. Rheological Properties of Semidilute and Concentrated Aqueous-Solutions of Cetyltrimethylammonium Bromide in the Presence of Potassium-Bromide. *Langmuir* **1989**, *5*, 1225−1229.
(77) Kern, F.; Zana, R.; Candau, S. J. Rheological Properties of Semidilute and Concentrated Aqueous-Solutions of Cetyltrimethylammonium Chloride in the Presence of Sodium-Salicylate and Sodium-Chloride. *Langmuir* **1991**, *7*, 1344−1351.
(78) Cates, M. E.; Candau, S. J. Statics and Dynamics of Worm-Like Surfactant Micelles. *J. Phys.: Condens. Matter* **1990**, *2*, 6869−6892.

CDV

(79) Cates, M. E. Reptation of Living Polymers − Dynamics of Entangled Polymers in the Presence of Reversible Chain-Scission Reactions. *Macromolecules* **1987**, *20*, 2289−2296.
(80) Turner, M. S.; Cates, M. E. Linear Viscoelasticity of Living Polymers—A Quantitative Probe of Chemical Relaxation-Times. *Langmuir* **1991**, *7*, 1590−1594.
(81) Han, C. D.; Kim, J. K. On the Use of Time−Temperature Superposition in Multicomponent Multiphase Polymer Systems. *Polymer* **1993**, *34*, 2533−2539.
(82) Kern, F.; Lemarechal, P.; Candau, S. J.; Cates, M. E. Rheological Properties of Semidilute and Concentrated Aqueous-Solutions of Cetyltrimethylammonium Bromide in the Presence of Potassium-Bromide. *Langmuir* **1992**, *8*, 437−440.
(83) Khatory, A.; Lequeux, F.; Kern, F.; Candau, S. J. Linear and Nonlinear Viscoelasticity of Semidilute Solutions of Wormlike Micelles at High-Salt Content. *Langmuir* **1993**, *9*, 1456−1464.
(84) Shukla, A.; Fuchs, R.; Rehage, H. Quasi-anomalous diffusion processes in entangled solutions of wormlike surfactant micelles. *Langmuir* **2006**, *22*, 3000−3006.
(85) Ng, W. K.; Tam, K. C.; Jenkins, R. D. Lifetime and network relaxation time of a HEUR-C20 associative polymer system. *J. Rheol.* **2000**, *44*, 137−147.
(86) Granek, R.; Cates, M. E. Stress-Relaxation in Living Polymers—Results from A Poisson Renewal Model. *J. Chem. Phys*. **1992**, *96*, 4758−4767.
(87) Granek, R. Dip in G″(ω) of Polymer Melts and Semidilute Solutions. *Langmuir* **1994**, *10*, 1627−1629.
(88) Morrison, F. A. *Understanding Rheology;* Oxford University Press: New York, 2001.
(89) Arratia, P. E.; Thomas, C. C.; Diorio, J.; Gollub, J. P. Elastic instabilities of polymer solutions in cross-channel flow. *Phys. Rev. Lett.* **2006**, *96*, 144502.
(90) Goddard, J. D. Material instability in Complex Fluids. *Annu. Rev. Fluid Mech.* **2003**, *35*, 113−133.
(91) Brown, E. F.; Burghardt, W. R.; Venerus, D. C. Tests of the Lodge-Meissner relation in anomalous nonlinear step strain of an entangled wormlike micelle solution. *Langmuir* **1997**, *13*, 3902−3904.
(92) Marrucci, G.; Ianniruberto, G. Effect of flow on topological interactions polymers. *Macromol. Symp.* **1997**, *117*, 233−240.
(93) Marrucci, G.; Greco, F.; Ianniruberto, G. Rheology of polymer melts and concentrated solutions. *Curr. Opin. Colloid Interface Sci.* **1999**, *4*, 283−287.
(94) Marrucci, G.; Ianniruberto, G. Open problems in tube models for concentrated polymers. *J. Non-Newtonian Fluid Mech.* **1999**, *82*, 275−286.
(95) Ianniruberto, G.; Marrucci, G. Convective orientational renewal in entangled polymers. *J. Non-Newtonian Fluid Mech.* **2000**, *95*, 363−374.
(96) Ianniruberto, G.; Marrucci, G. A simple constitutive equation for entangled polymers with chain stretch. *J. Rheol.* **2001**, *45*, 1305−1318.
(97) Marrucci, G.; Greco, F.; Ianniruberto, G. Integral and differential constitutive equations for entangled polymers with simple versions of CCR and force balance on entanglements. *Rheol. Acta* **2001**, *40*, 98−103.
(98) Mead, D. W.; Larson, R. G.; Doi, M. A molecular theory for fast flows of entangled polymers. *Macromolecules* **1998**, *31*, 7895−7914.
(99) Likhtman, A. E.; Milner, S. T.; Mcleish, T. C. B. Microscopic theory for the fast flow of polymer melts. *Phys. Rev. Lett*. **2000**, *85*, 4550−4553.
(100) Milner, S. T.; Mcleish, T. C. B.; Likhtman, A. E. Microscopic theory of convective constraint release. *J. Rheol.* **2001**, *45*, 539−563.
(101) Whorlow, R. W. *Rheological Techniques;* Halsted Press: Chichester, 1980.
(102) Britton, M. M.; Callaghan, P. T. Shear banding instability in wormlike micellar solutions. *Eur. Phys. J. B* **1999**, *7*, 237−249.
(103) deGennes, P. G. Tortured Chains: An Introduction. In *Flexible Polymer Chains in Elongational Flow*; Nguyen, T. Q., Kaussch, H. H., Eds.; Springer: Berlin, 1999; pp 1−3.
(104) Kadoma, I. A.; van Egmond, J. W. Flow-induced nematic string phase in semidilute wormlike Micelle solutions. *Phys. Rev. Lett.* **1998**, *80*, 5679−5682.
(105) Kadoma, I. A.; van Egmond, J. W. Shear-enhanced orientation and concentration fluctuations in wormlike micelles: Effect of salt. *Langmuir* **1997**, *13*, 4551−4561.
(106) Hashimoto, T.; Kume, T. Butterfly Light-Scattering Pattern in Shear-Enhanced Concentration Fluctuations in Polymer-Solutions and Anomaly at High Shear Rates. *J. Phys. Soc. Jpn.* **1992**, *61*, 1839−1843.
(107) Moses, E.; Kume, T.; Hashimoto, T. Shear Microscopy of the Butterfly Pattern in Polymer Mixtures. *Phys. Rev. Lett*. **1994**, *72*, 2037−2040.
(108) Hobbie, E. K.; Lin-Gibson, S.; Wang, H.; Pathak, J. A.; Kim, H. Ubiquity of domain patterns in sheared viscoelastic fluids. *Phys. Rev. E* **2004**, *69*, 061503.
(109) Rubinstein, M.; Colby, R. H. *Polymer Physics;* Oxford University Press: New York, 2003.
(110) deGennes, P. G. *Scaling Concepts in Polymer Physics;* Cornell University Press: Ithaca, NY, 1979.
(111) Doi, M.; Edwards, S. F. *The Theory of Polymer Dynamics;* Clarendon Press: Oxford, UK, 1986.

MA061355R